

Assembly of fluorophore J-aggregates with nanospacer onto mesoporous nanoparticles for enhanced photoacoustic imaging

Wujun Xu, Jarkko Leskinen, Teemu Sahlström, Emilia Happonen, Tanja Tarvainen, Vesa-Pekka Lehto*

Department of Technical Physics, University of Eastern Finland, 70210 Kuopio, Finland

ARTICLE INFO

Keywords:

Nanoparticles
Contrast agents
Imaging
Photoacoustics
Nanospacer
Mesoporous silicon
Laser
J-aggregates

ABSTRACT

Many fluorophores, such as indocyanine green (ICG), have poor photostability and low photothermal efficiency hindering their wide application in photoacoustic (PA) tomography. In the present study, a supramolecular assembly approach was used to develop the hybrid nanoparticles (Hy NPs) of ICG and porous silicon (PSi) as a novel contrast agent for PA tomography. ICG was assembled on the PSi NPs to form J-aggregates within 30 min. The Hy NPs presented a red-shifted absorption, improved photothermal stability, and enhanced PA performance. Furthermore, 1-dodecene (DOC) was assembled into the NPs as a ‘nanospacer’, which enhanced non-radiative decay for increased thermal release. Compared to the Hy NPs, adding DOC into the Hy NPs (DOC-Hy) increased the PA signal by 83%. Finally, the DOC-Hy was detectable in PA tomography at 1.5 cm depth in tissue phantom even though its concentration was as low as 6.25 $\mu\text{g}/\text{mL}$, indicating the potential for deep tissue PA imaging.

1. Introduction

Photoacoustic (PA) imaging is a hybrid imaging modality in which the absorption of externally introduced light creates local heating that produces ultrasonic waves for acoustic imaging [1,2]. PA imaging has a much higher spatial resolution in deep tissue than optical imaging because biological tissue is more transparent to sound than to light [3]. It has wide applications in imaging soft biological tissues, such as blood vessels and microvasculature of tumours in medical imaging, and for small animal imaging in biomedical applications [4,5].

Various nanoparticles (NPs) have been developed as contrast agents for enhancing PA imaging [6–8]. Molecular packing of fluorophore in these NPs plays a critical role to affect their performance in PA imaging. ‘‘Face-to-face’’ packing leads to H-aggregates while ‘‘head-to-tail’’ packing, i.e., slip-stacked alignment of fluorophore, constructs J-aggregates. J-aggregates generate unique photophysical properties, such as red-shifted absorption spectra and enhanced quantum yields [9,10]. Thus, the molecular packing as J-aggregates is more favored than that of H-aggregates for photo-based biomedical applications. Indocyanine green (ICG), approved by US Food and Drug Administration (FDA) for clinical applications, is widely applied in photo-based therapeutics [11–13]. However, it has poor photostability and thus its imaging

performance declines fast with the prolonged laser illumination. Besides, the ICG molecule has a planar conformation and it favors a strong face-to-face π - π stacking [14–17]. Accordingly, the formation of H-aggregation is found most commonly in different ICG NPs for photothermal-based applications [14–17]. For example, ICG was loaded into porous silicon (PSi) NPs via calcium silicate-based sealing chemistry. Several special features of PSi, such as high surface area, good biocompatibility [18,19], and low thermal conductivity [20], make it a good carrier for the delivery of ICG. Thus, the ICG NPs presented enhanced performance in PA imaging and photostability as compared to the liposome-ICG formulation [20]. However, NPs possessed the same absorption peak at 780 nm as free ICG molecules, indicating that ICG was still presented as H-aggregates in NPs [20]. On the other hand, ICG J-aggregates were developed for PA imaging with a long-time heating period (~ 65 °C for more than 24 h) [21,22], which is time-consuming and is not suitable to prepare multifunctional NPs with temperature-sensitive components such as proteins, peptides and antibodies. Thus, there is a need to develop a simple and fast approach for preparing ICG J-aggregates NPs for PA imaging.

In addition to the packing form of fluorophore, the PA effect of contrast agents is also dependent on several other parameters including Grüneisen coefficient and the efficiency of non-radiative decay [1,23].

* Corresponding author.

E-mail address: vesa-pekka.lehto@uef.fi (V.-P. Lehto).

<https://doi.org/10.1016/j.pacs.2023.100552>

Received 1 December 2022; Received in revised form 23 May 2023; Accepted 26 August 2023

Available online 28 August 2023

2213-5979/© 2023 The Authors. Published by Elsevier GmbH. This is an open access article under the CC BY-NC-ND license (<http://creativecommons.org/licenses/by-nc-nd/4.0/>).

As compared to gold NPs with a similar absorption coefficient, the strong thermal confinement effect of the polymer NPs enhanced the generation efficiency of PA signal, which could be improved by the increase of the Grüneisen parameter of the NPs [24]. Furthermore, the control of the intramolecular motion was proposed as a good approach for efficient non-radiative decay resulting in enhanced photothermal heating for PA imaging [25–27]. In these studies, the compounds with a long alkyl chain were chemically conjugated onto fluorophores as ‘nanospacer’ to create extra free space for efficient intramolecular motion. Despite the promising performance in PA imaging, the chemical processes to covalently conjugate the nanospacer requires multiple reaction steps, a long reaction time (> 24 h), and many toxic chemicals for reaction and purification [27,28]. Thus, up to now, none of the studies have been published to promote the intramolecular motion of ICG molecules with the ‘nanospacer’ approach.

The present study aims to develop ICG-PSi hybrid (Hy) NPs as a highly efficient PA contrast agent by combining the strategies of J-aggregates and ‘nanospacer’ via a simple and fast supramolecular assembly approach. The Hy NPs are prepared by the assembly of ICG onto PSi as J-aggregate with amine silane-assisted metal-ion coordination. The assembled Hy NPs with Zn^{2+} present the highest PA signal as compared to the counterparts with Ca^{2+} and Fe^{3+} , and Cu^{2+} . Furthermore, a nanospacer, 1-dodecene (DOC), with a long alkyl chain was expected to realize the intermolecular spatial isolation of the ICG molecules in the J-aggregate state to promote free intramolecular motion, boosting non-radiative decay process for enhanced PA performance. With the coating of bovine serum albumin (BSA), the NPs present good colloidal stability and biocompatibility. Compared with the complicated approach of chemical conjugation [25,26], the non-covalent supramolecular assembly is simple, fast, and efficient to enhance the performance of ICG in PA imaging.

2. Materials and methodology

2.1. Materials

Sodium silicide (NaSi) was kindly provided by SiGNa Chemistry Inc. ICG, sodium bromide (NaBr, 99%), ammonium bromide (NH_4Br , 99%), hydrogen fluoride (HF, 37%), hydrochloric acid (HCl, 37%), 3-(2-aminoethylamino) propyldimethoxymethylsilane (AEAPMS), BSA, calcium chloride ($CaCl_2$), iron (III) chloride ($FeCl_3$), and copper Sulfate ($CuSO_4$), DOC, and paclitaxel (PTX) were purchased from Sigma-Aldrich. Perfluoro-1-dodecene (PFD) was ordered from Alfa Aesar. Phosphate buffer saline (PBS, pH = 7.4) was bought from VWR. The CellTiter Glo cell luminescent viability assay was bought from Promega. All reagents were used directly as received.

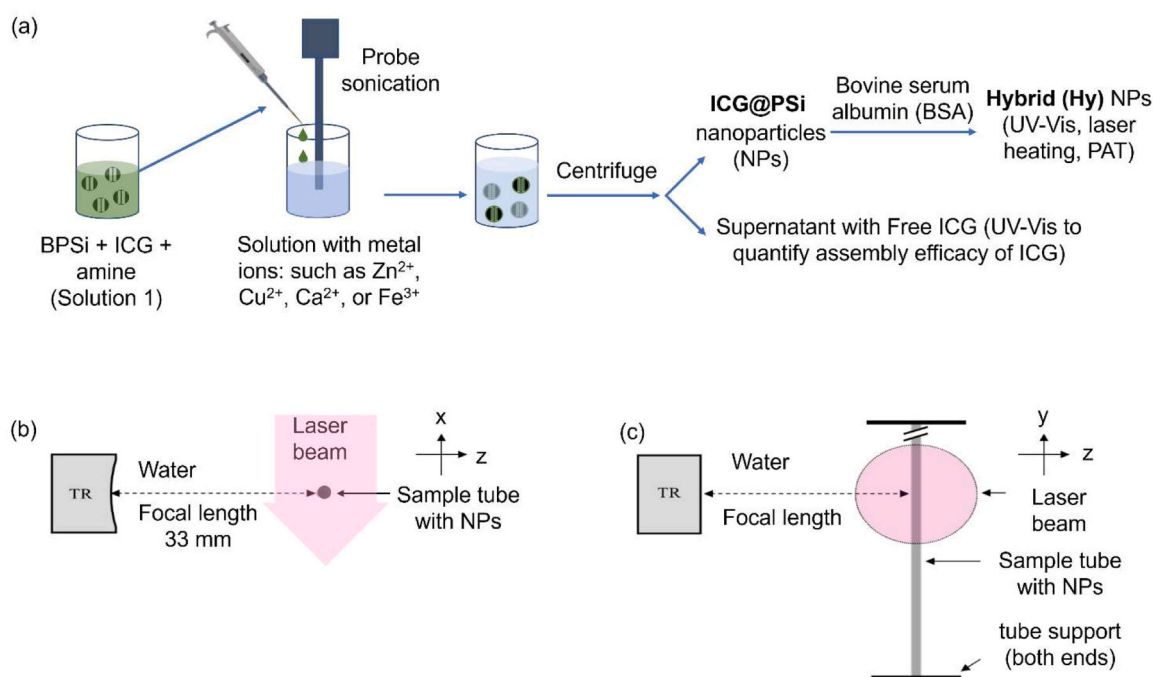
2.2. Preparation of NPs

2.2.1. PSi NPs

NaSi, NH_4Br , and NaBr were mixed with the mass ratio of 1/4/4 and then reacted at 250 °C in N_2 atmosphere [29,30]. After cooled to ambient temperature (25 °C), the raw product was rinsed with 1.0 M HCl twice, purified with 5% HF, and dried at 65 °C. The particles were milled (1000 rpm) in ethanol to prepare the PSi NPs with a planetary ball mill (Fritsch Pulverisette 7).

2.2.2. Assembly of ICG on PSi to prepare Hy NPs

The supramolecular assembly approach was utilized to prepare the Hy NPs (Scheme 1a). In a typical experiment: 0.30 mg PSi NPs were mixed with 0.15 mg ICG in 0.5 mL methanol (noted as PSi-ICG mix) and then amine silane 3-(2-aminoethylamino) propyldimethoxymethylsilane (AEAPMS) was added (Solution 1). Next, the solution 1 was added into 0.5 mL 0.4 M aqueous solution of Zn^{2+} drop by drop under probe sonication with ice cooling. The amplitude was set at 40% and a continuous sonication model was applied (Hielscher, UP400S). The solution was stirred at room temperature for 15 min. The NPs were recovered by centrifuge, washed with deionized H_2O , and redispersed in



Scheme 1. (a) Illustration to prepare hybrid nanoparticles (NPs); (b, c) Setup for photoacoustic signal measurement using the plastic tube as a NP insert. (b) Side view of the system indicating the positions of the ultrasound transducer (TR), tube, and laser beam. The transducer and tube were immersed in water during measurement. (c) Top view of the setup.

1.0 mL H₂O. The obtained samples were noted as ICG@PSi NPs. At the end, 0.3 mL BSA solution with a concentration of 20 mg/mL was added slowly into the suspension of ICG@PSi NPs under probe sonication. The final product (noted as Hy NPs) was recovered by centrifuge and rinsed with H₂O. To study the effect of metal ions on the PA effect, also other metal ions, including Ca²⁺, Fe³⁺, and Cu²⁺, were used to prepare Hy NPs. The experiment protocol was the same as described above.

ICG concentration in the NPs suspension before and after experiments was measured with UV-Vis. The assembly efficacy of ICG was calculated according to the following equation:

$$\text{ICG assembly efficacy} = 100\% \cdot \frac{C_0 - C}{C_0}$$

where C_0 and C are the concentrations of free ICG in the solution before and after supramolecular assembly, respectively.

2.2.3. Preparation of NPs with activated intramolecular motion

DOC was used as the nanospacer to promote the intramolecular motion of ICG. The NPs were prepared with the same protocol as described for ICG-PSi Hy NPs except DOC was added into the solution 1. Two other compounds PTX and PFD were used as the references of the nanospacer. The obtained NPs are noted as DOC-Hy, PTX-Hy, and PFD-Hy, respectively.

2.3. Physicochemical characterizations

The porous parameters of the PSi NPs were measured with N₂ adsorption/desorption experiments (Tristar II 3020, Micromeritics) at 77 K. The multiple-point Brunauer–Emmett–Teller (BET) method was used to calculate the surface area. The light absorption spectra of the samples were measured with a UV–Vis spectrophotometer. 0.5 mL of the NP suspension with a pre-determined concentration was placed in a quartz cuvette and the light absorption was measured in the 500 – 1000 nm range.

The particle diameter and zeta potential of the NPs were measured in H₂O at 25 °C using Malvern ZetaSizer Nano ZS (Malvern Instruments, U. K.). Fourier Transform Infrared (FTIR) spectroscopy (ThermoNicolet spectrometer) was used to confirm the chemical composition of the NPs. The experiments were performed with an attenuated total reflection (ATR) model of the instrument.

The morphology of the NPs was characterized by transmission electron microscopes (TEM) (JEOL 2010). A drop of the NPs suspension was placed on a carbon-coated Cu grid and then the solvent was evaporated at ambient temperature before taking the TEM images.

The colloidal stability of the NPs was measured by monitoring the diameter of the NPs in PBS. The sample was incubated at 37 °C for different time periods and the diameter of the sample was measured with ZetaSizer Nano ZS (Malvern) at 25 °C.

The laser heating tests were carried out to evaluate the photothermal conversion performance of samples. 1.0 mL suspension of the samples were added into DLS cuvettes and irradiated with 808 nm laser (PL-808–1000, SKY Laser 1.0 W power). The temperature change of the suspension was measured with a K-type thermocouple.

2.4. Measurement of PA signal

The photoacoustic measurement setup consisted of a Nd:YAG laser (neodymium-doped yttrium aluminum garnet) and optical parametric oscillator (model NT352B-10; Ekspla Uab, Lithuania) which provided 3 ns long pulses at 808 nm wavelength and at a repetition rate of 10 Hz. The pulses were guided to an optical fiber, expanded using the planoconvex lens, and then shaped to approximately a flat-top profile using an engineered diffuser (model EDC-5; RPC Photonics, NJ, USA). Photoacoustic waves were detected using a circular cylindrically focused PZT transducer (model V383; Olympus NDT, MA, USA) connected to

pulser-receiver (model 5800PR; Olympus) providing filtering (0.1–10 MHz) and signal amplification (40 dB) (Scheme 1b). The transducer has 3.4 MHz center frequency, – 6 dB bandwidth from 1.7 to 5.1 MHz, 9.5 mm element diameter, and 33 mm focal length. Photoacoustic data was measured using an oscilloscope (model 6051 A WR; LeCroy Inc., NY, USA). The laser pulse energy was measured prior to the experiments using a pyroelectric sensor and energy meter (models PE50BF-C and StarBright, respectively; Ophir Photonics, UT, USA). To correct laser pulse fluctuation, relative laser pulse energy for each captured photoacoustic waveform was measured using a photodiode detector (model PDA10A2; Thorlabs, NJ, USA) which captured a laser reflection from the planoconvex lens. Photodetector was connected to the second oscilloscope channel.

The photoacoustic signal level of different samples of NPs was measured in controlled water environment. Samples of deionized degassed water and India ink were used as references (supporting information). Disposable plastic microcapillary tubes (PETG; Globe Scientific, NJ, USA) were used to load the samples. The tubes have an outer diameter, inner diameter, and length of 1.55 mm, 0.85 mm, and 75 mm, respectively. The transducer focal point was directed on the side of the tube (Scheme 1b and c). Focal point was aligned to the tube using pulse-echo measurements and photoacoustic signal detection prior to the experiments. The water tank was filled with deionized and degassed water ($T = 20.1 \pm 0.3$ °C). Laser beam diameter on the target surface was approximately 20 mm ($1/e^2$ value). An average laser pulse energy was 1.52 ± 0.03 mJ (mean \pm standard deviation) when measured with energy meter in air. A total of 50 acoustic waveforms were measured for each sample which were then averaged to give the final waveform for the sample. Oscilloscope sampled the waveforms at 1 GHz sampling frequency. Each NP sample was measured three times and a new sample was prepared for each repeat. Final PA signal amplitude for each sample was calculated as peak-to-peak voltage (Vpp) of averaged acoustic waveform and corrected with photodetector signal (Fig. S1, supporting information).

2.5. Tomographic imaging of tissue phantom

The performances of the samples were evaluated through tomographic imaging of tissue phantom consisting of thin-walled plastic tubing that contained the suspension of NPs placed inside chicken tissue and casted inside gelatine. The tubing was clear polyvinyl chloride (PVC) tube and had 1.2 mm outer diameter, 0.8 mm inner diameter, and 800 mm length (Reichelt Chemietechnik, Germany). The tube was twisted into a loop having an inner diameter of 5 mm. The fresh chicken filet was cut to approximately 3 cm \times 3 cm \times 3 cm (width \times length \times height) piece. Small incision was cut in the piece so that tubing could be placed in the middle of the tissue. The depth of tubing in the tissue was 1.5 cm in the final phantom. Tissue was then placed in degassed water and degassed in a vacuum chamber for 1 h to remove trapped air bubbles. Porcine gelatine powder (200 bloom; Sigma Aldrich, MO, USA) was mixed with hot water to make 8% gelatine solution and degassed. Chicken tissue was quickly moved into gelatine and re-degassed, and the tissue phantom was casted using a mould.

An estimated volume of tubing was 400 μ L. To fill the tube fully and evenly, an excessive amount of NP solution (2 mL) was pumped and wasted through tubing using a syringe before the tube was deduced to be filled. When the sample was changed, the tube was emptied and cleaned with clean compressed air, 70% ethanol-water solution, and deionized water. Reference measurements between the NP measurements using water sample indicated that this cleaning protocol was adequate as the signal from water-filled tubing was low. It also verified that the tube itself was not a strong photoacoustic source.

During the measurements, the phantom was placed in degassed deionized water ($T = 19.9 \pm 0.2$ °C). The water layer above the phantom was approximately 5 mm. The ultrasound sensor was rotated 270 degrees with increments of 1 degree using the rotation stage (model

8MR151–30; Standa Uab, Lithuania). The average laser pulse energy was 11.7 mJ and estimated fluence at tissue surface was 5 mJ/cm² which is below maximum permissible exposure for skin at this wavelength [International Electrotechnical Commission, Safety of laser products—part 1: Equipment Classification and Requirements (Geneva, Switzerland: IEC-60825–1, edition 3, 2014)]. At each angle total of 16 waveforms were recorded, averaged, and stored using oscilloscope at 500 MHz sampling. Waveform corrected with laser energy fluctuation measured with the photodetector in second oscilloscope channel was fed into reconstruction algorithm. A laptop computer running LabView software (National Instruments, TX, USA) controlled the measurement.

A photoacoustic image was reconstructed from measured photoacoustic signals using a Bayesian approach to inverse problems [23,31]. In PA tomography, the reconstructed image is the initial pressure p_0 created by the photoacoustic effect. It is obtained by minimising

$$\min_{p_0} -\frac{1}{2} \|L_e(p_t - Kp_0 - \eta_e)\|^2 - \frac{1}{2} \|L_{p_0}(p_0 - \eta_{p_0})\|^2$$

where p_t is the measured photoacoustic data and K is a discretised forward operator that describes ultrasound propagation in the target. In the present work, ultrasound propagation was modelled with the acoustic wave equation which was numerically solved using a k -space time-domain method implemented with the k-Wave MATLAB toolbox [32]. Further, η_e and L_e describe noise statistics, and η_{p_0} and L_{p_0} statistics of the prior information that is needed in the solution of an inverse problem to alleviate the ill-posedness.

For the inverse problem, the 70.6 × 70.6 × 9.5 mm (reconstruction) domain was discretized in 500 × 500 × 68 voxels with a voxel size of $\Delta x = 141 \mu\text{m}$. Temporal discretization of $N_t = 1654$ time points with a time step of $\Delta t = 28.2$ ns was used. The transducer response was modelled by dividing the surface of the transducer into approximately 4000 elements (corresponding to the voxels on the transducer surface) and averaging the signal for all elements. Furthermore, the frequency response of the transducer was considered by filtering the signals using the frequency response provided by the transducer manufacturer. Statistics (mean and standard deviation) of the measurement noise were determined from a signal preceding the illumination for each sensor. The prior distribution was the Ornstein-Uhlenbeck prior distribution with the mean, standard deviation, characteristic length of $\eta_{p_0} = 0$, $\sigma_{p_0} = 0.01$, and $l = 80 \mu\text{m}$. The minimisation problem above was solved utilising a matrix free form using MATLAB in-built generalized minimum residual method.

2.6. Cell viability test

MDA-MB-231 cells (10⁴ per/well, 100 μL) were cultured on 96-well plates with the medium of RPMI-1640 (Biowest) containing 10% fetal bovine serum (Sigma). NPs were washed with deionized H₂O and then dispersed in cell medium with desired concentration. Prior to adding the NPs, the cells were washed with Hank's balanced salt solution (HBSS) three times. The cells were incubated with the different concentrations of the NPs for 4 h, then rinsed with fresh medium, and cultured for an extra 20 h. Then, cell viability was measured with the CellTiter Glo® assay according to the instruction from the manufacturer (Promega Corp.).

3. Results and discussions

3.1. Assembly of ICG J-aggregates in Hy NPs

The PSi NPs presented IV isotherm type with H1 hysteresis in the N₂ adsorption/desorption experiment, showing the presence of mesoporous structure (Fig. S2, supporting information). The PSi had a surface area of 176.7 m²/g, the pore size of 8.9 nm, and pore volume of 0.48 cm³/g. Thus, the PSi could act as a large 'reservoir' to load different cargos due to its large pore volume. ICG molecule has two sulfonate anions at each

terminal, and thus it can coordinate with some metal ions to form poorly soluble nanoaggregates, which was utilized as the mechanism to assemble ICG into PSi. The assembly efficacy of ICG was as high as 95% while it was lower than 30% in the absence of amine-silane AEAPMS, indicating that AEAPMS assisted the assembly of ICG in the Zn²⁺ coordination process. Many other organic compounds with amine groups such as dipicolylamino (DPA) have been used to promote the loading of ICG [33,34]. Amine silane AEAPMS offers several benefits in the assembly of ICG into PSi as compared to DPA. First, DPA is an aromatic amine, and it has two benzene rings in its chemical structure while AEAPMS has a linear alkyl chain. It has been well proven that most compounds with aromatic amines have the potential to cause diseases such as cancer [35]. Second, the benzene rings of DPA may also tend to form a strong π - π interaction with ICG, hindering the intramolecular motion of ICG. Third, AEAPMS has a siloxane bond (Si-O-C) on the other side of the molecule, which favors the hydrolyzation as Si-OH in an aqueous environment. Thus, the ICG nanoaggregates are terminated with -OH, which is beneficial to form the hydrogen bond interaction between the Si-OH groups on the PSi NPs.

The UV-Vis spectra (Fig. 1a) show that the self-assembly of ICG on the ICG@PSi and Hy NPs caused the red-shift of the absorption peak and significantly enhanced light absorption as compared to the free ICG. The specific absorption peak of free ICG was around 780 nm while it shifted to 807 nm in the Hy NPs. Calculated with the Lambert-Beer law, the mass extinction coefficient of Hy NPs was 123.1 L g⁻¹ cm⁻¹ at 808 nm which was almost 4 times the value for the free ICG (32.8 L g⁻¹ cm⁻¹), respectively. The absorption redshift and enhanced absorption of the NPs indicate the formation of J-aggregates with the slip-stacked alignment of the ICG molecule [26].

The photothermal conversion efficiency of different samples is shown in Fig. 1b. The poor photostability of ICG is one of the main drawbacks to prevent its wide applications in photo-based therapeutics. For example, photobleaching of ICG limits its detectability, shortens observation time, and leads unstable imaging performance. The free ICG presented a declining photothermal curve after 3.5 min laser illumination while both the ICG@PSi and Hy NPs have enhanced photothermal conversion efficacy and photothermal stability. Among these samples, the Hy NPs presented the best performance in photothermal test. The temperature increase of the Hy NPs is nearly two times of that with free ICG with the same concentration. Thus, the assembly of ICG into the PSi NPs significantly enhanced both the photostability and photothermal conversion as compared to free ICG.

PA signals are shown in Fig. 1c-f. The Hy NPs presented 1.78- and 1.66-times higher amplitude regarding PA signal than free ICG and the physical mixture of PSi+ICG, respectively (Fig. 1c). It has been demonstrated that transition metal ions had a major effect on the PA performance of fluorophores due to the influence of electron transfer [36]. Thus, different diamagnetic metal ions (Ca²⁺ and Zn²⁺) and paramagnetic ions (Fe³⁺ and Cu²⁺) were studied (Fig. 1d). Among these tested ions, Zn²⁺-based Hy NPs possessed the best PA performance. Using Ca²⁺, Cu²⁺, and Fe³⁺ caused a negative effect on their PA signal of the Hy NPs compared to the physical mixture of PSi+ICG. Previous study has shown that diamagnetic metal ions, such as Mg²⁺ and Zn²⁺, may enhance fluorescence and decrease photothermal performance of fluorophore while paramagnetic metal ions, such as Cu²⁺ and Co²⁺, would lead to a contrary effect, i.e., quenched fluorescence and increased photothermal heating [37]. However, this phenomenon is dye-specific because the chemistry property of dye may also have an important effect on photothermal performance. ICG can be photobleached easily by photoinduced oxidation process, which means that ICG is sensitive to oxidants. Among the studied metal ions, the order of oxidative capacity is Fe³⁺>Cu²⁺>Zn²⁺>Ca²⁺ [38]. Ca²⁺ has a low standard electrode potential (Ca²⁺ + 2e⁻ = Ca, E⁰ = -2.84 V [38]) which is inefficient for the electron-transfer process. Thus, Fe³⁺-based Hy NPs had the lowest PA signal while Zn²⁺ based Hy NPs presented the best results in Fig. 1d.

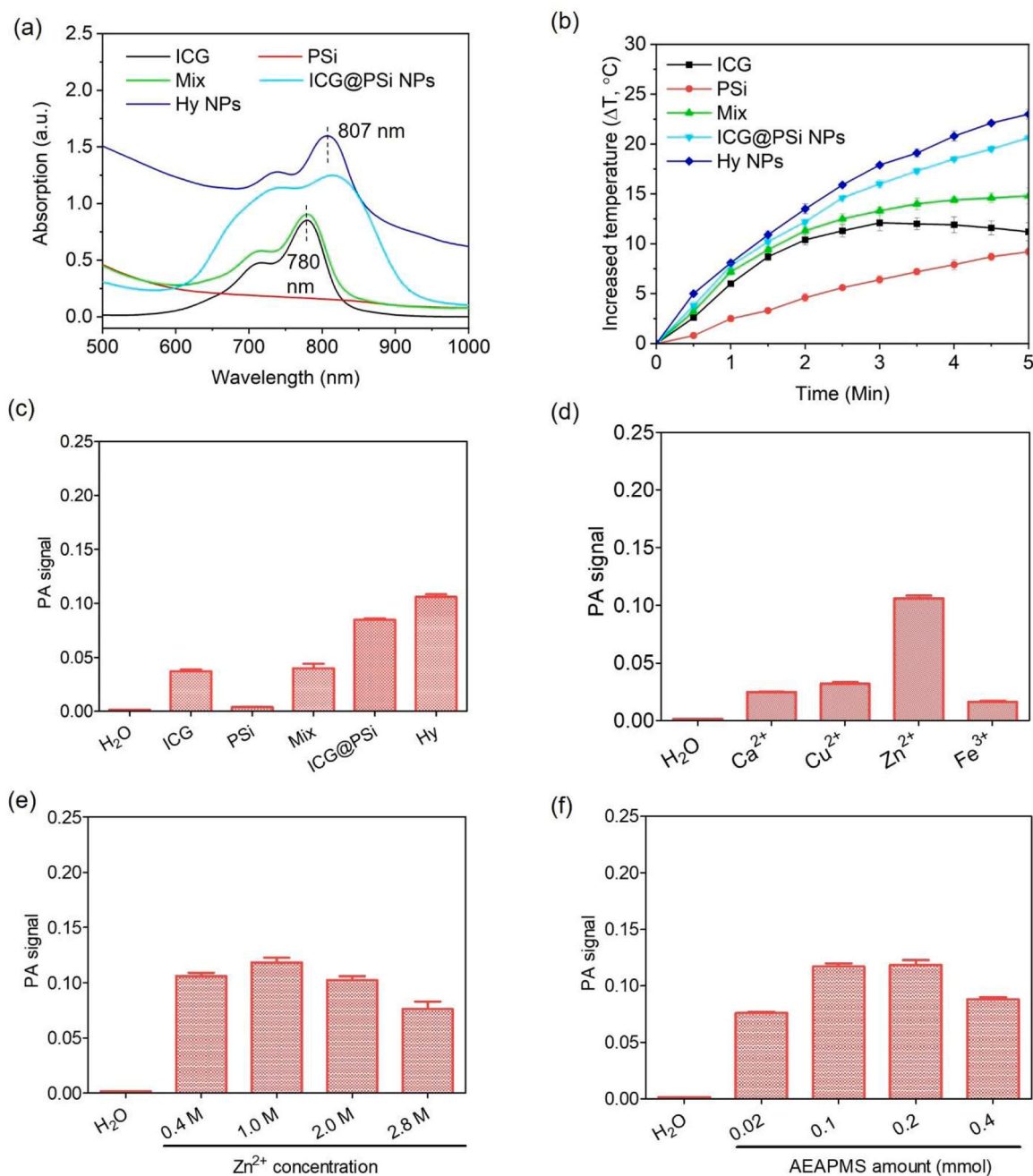


Fig. 1. (a) UV-Vis absorption spectra, (b) photothermal heating profiles, and (c) photoacoustic (PA) signal of H₂O, free ICG, PSi, PSi+ICG mix, ICG@PSi and Hy NPs. The concentration of ICG was 6.25 μg/mL in UV-Vis measurements because it exceeds the measurement range in the samples of PSi-ICG mixture and Hy NPs with the concentration of 12.5 μg/mL; (d-f) PA signal of Hy NPs in optimizing the effect of (d) ion types, (e) Zn²⁺ concentration, and (f) AEAPMS amount. The concentration of ICG in (b-f) was 12.5 μg/mL. H₂O sample was used as the control group.

Next, the preparation of the Hy NPs was further optimized by studying the effect of Zn²⁺ concentration (Fig. 1e) and AEAPMS amount (Fig. 1f). Increasing the concentration of Zn²⁺ from 0.4 to 1.0 M did not significantly enhance the intensity of the PA signal while the further increase of the Zn²⁺ concentration above 2.0 M caused the decrease of the PA signal. On the other hand, the PA signal of the Hy NPs first increases when increasing the amount of AEAPMS from 0 to 0.1 mM. Then, the PA signal was almost identical to the sample prepared with 0.2 mM AEAPMS, and finally turns to decline with 0.4 mM AEAPMS. Tuning these parameters did not cause the shift of absorption peak in UV-Vis spectra. The change of absorption intensity in UV-Vis spectra is consistent with that observed in the PA signal (Figs. S3 and S4, supporting information). Thus, 1.0 M Zn²⁺ concentration and 0.1 mmol

AEAPMS are optimal for the preparation the Hy NPs.

3.2. Preparation and characterization of DOC-Hy NPs

Steric hindrance due to the neighboring molecules may restrict intramolecular motions, inhibiting the photothermal conversion of the NPs. A previous study demonstrated that chemical conjugation of fluorophore compound with an alkyl chain can promote free intramolecular motion, boosting non-radiative decay for enhanced photothermal conversion [26]. Thus, we hypothesize that the same outcome can be achieved by adding DOC which has 12 carbon atoms in the alkyl chain as the ‘nanospacer’ in the supramolecular assemble of the DOC-Hy NPs (Fig. 2a).

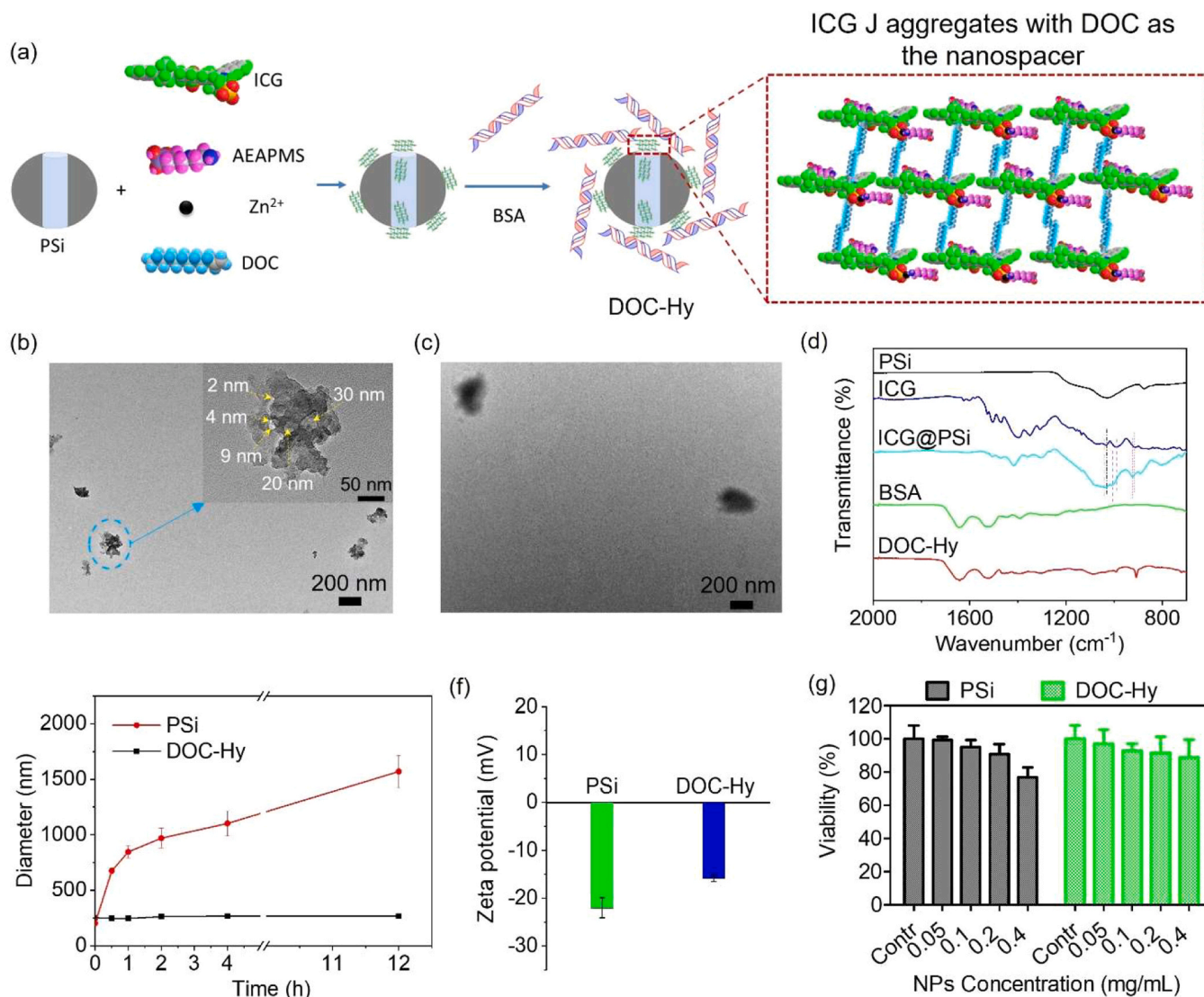


Fig. 2. (a) Scheme to illustrate the preparation of DOC-Hy NPs via ‘one-pot’ assembly approach. 1-dodecene (DOC) with a linear alkyl chain was used as the ‘nanospacer’. (b-g) Physicochemical characterization of NPs: TEM images of (b) PSI NPs. Inset shows the corresponding high-resolution of PSI with porous structure and (c) DOC-Hy; (d) FT-IR spectra of PSI, free ICG, Hy NPs, free BSA, and DOC-Hy NPs; (e) colloidal stability, (f) surface charge, and (g) viability of MDA-MB-231 cells after incubated with PSI and DOC-Hy NPs.

The shape of the NPs is shown in the TEM images (Fig. 2b, c). The initial PSI NPs have an irregular shape with the diameter around 200 nm and present a porous structure with the pore size in the range of 2–30 nm (Fig. 2b). After the assembly of ICG, DOC, and BSA onto the PSI, a core-shell structure is observed in the TEM image of the DOC-Hy NPs (Fig. 2c). The dark core is from the ICG-loaded PSI while the shell is made of BSA coating. As compared to the NPs without BSA coating (Fig. S5, supporting information), the TEM images of the DOC-Hy NPs became fuzzy due to the protein coating of BSA. The diameter of the DOC-Hy NPs increased to ca. 250 nm. The composition of the NPs was characterized with ATR-FTIR (Fig. 2d). PSI NPs present the typical peak of Si-O bond at 1029 cm⁻¹ [18]. The aromatic C=C stretches (1504 and 1469 cm⁻¹), C-H vinyl stretches (917 and 988 cm⁻¹), and symmetric sulfonate (SO³⁻) vibrations from ICG are well-observed in the spectrum of ICG@PSi NPs [39,40], indicating that ICG was successfully assembled in the NPs. The major peaks of BSA appeared at 1645 and 1530 cm⁻¹, corresponding to amide I and amide II bonds in its protein structure. Due to the overlapping BSA peaks, the peaks of the functional groups in ICG and PSI were not easily visible in the FT-IR spectrum of Hy NPs.

Furthermore, the DOC-Hy NPs had several promising physicochemical features for biomedical applications. First, the NPs had good colloidal stability in PBS due to the coating of BSA (Fig. 2e). PSI and DOC-Hy NPs had an initial particle diameter around 202 and 254 nm, respectively. There was no significant change of particle diameter in Hy NPs when the sample was incubated in PBS at 37 °C for 12 h, whereas the diameter of PSI increased to 1500 nm under the same experiment condition. Second, the NPs have a negative zeta potential around -15.7 mV (Fig. 2f). A positive charge of NPs would promote the formation of hard protein corona when the NPs are injected into bloodstream, causing a quick clearance by immune cells [28]. Third, the DOC-Hy NPs have good biocompatibility (Fig. 2g). The cell viability results indicated that the NPs did not cause significant cytotoxicity even when the concentration was up to 0.4 mg/mL, which is comparable to the PSI with polyethylene glycol (PEG) coating [23]. In contrast, the plain PSI NPs decreased the cell viability when the high concentration of NPs was applied.

Fig. 3a shows the UV-Vis spectra of Hy NPs before and after adding different amounts of DOC. Adding DOC in the assembly process did not change the location of the absorption peak but enhanced its absorption

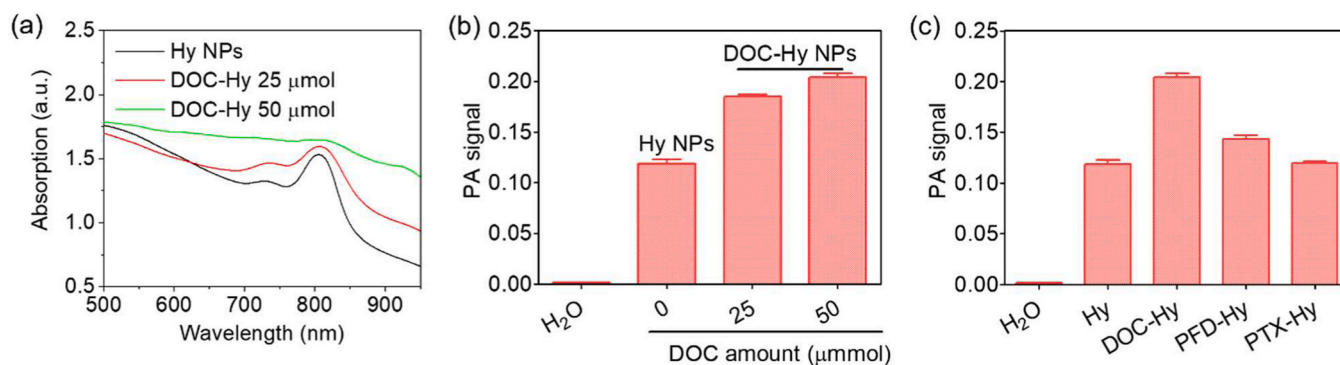


Fig. 3. (a) UV-Vis spectra, (b) PA signal of DOC-Hy NPs with different DOC amount, (c) Comparison of PA signal from DOC-Hy, PFD-Hy, and PTX-Hy NPs.

intensity. Fig. 3b shows the DOC-Hy NPs possess 83% higher PA signal than the Hy NPs. The comparison of PA signal between free ICG and DOC-Hy NPs is presented in Fig. S7 (Supporting information). To generate the PA signals with the same amplitude as 6.25 or 12.5 μg/mL DOC-Hy NPs, the required concentrations of free ICG were 38.86 and 78.04 μg/mL, respectively. The results are consistent with the hypothesis that adding nanopacer such as DOC can enhance PA performance of the NPs. As control experiments, two other compounds, PFD and PTX were studied as the references of the 'nanospacer' (Fig. 3c). PFD has the same length of the carbon chain as DOC, but the hydrogen atoms are replaced with fluorine. It may create a similar free space for

intramolecular space as DOC, however, it was less effective than DOC to enhance the PA signal of the NPs. This is probably due to the PFD has a bigger spatial hindrance due to the replacement of fluorine in its structure than DOC. On the other hand, PTX is a hydrophobic compound with aromatic rings in its structure, which tends to form strong π - π interaction with ICG. It cannot produce some necessary rooms to promote free intramolecular motion and thus it did not enhance the PA of the NPs.

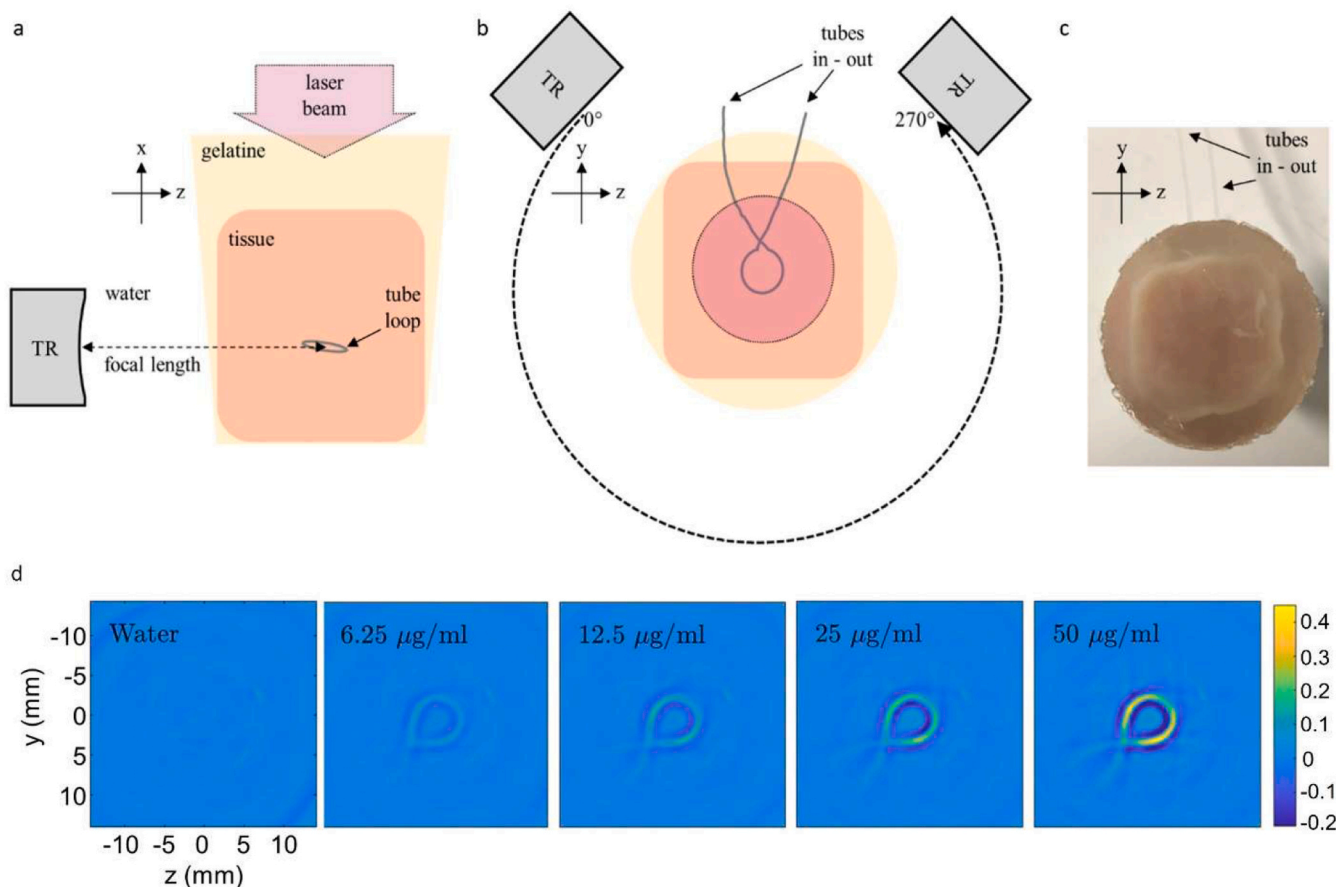


Fig. 4. (a)-(c) Scheme to illustrate the PA tomography measurement using permanently placed plastic tube inside chicken tissue and covered with gelatine. a) Side view of the system indicating the positions of the transducer, three-part phantom, and laser beam. Transducer and phantom were immersed in water during tomography (TR = ultrasound transducer). b) Top view of setup showing the span of rotation. The red circle with dotted edge shows the spot of the laser beam. c) Photo of phantom indicating the tube inlet and outlet. Tissue and gelatine boundaries are also clearly visible. (d) Cross sectional images from 3D reconstructions of the chicken tissue phantom with water and four DOC-Hy NP concentrations. The scale bar represents PA amplitude in the measurements.

3.3. PA tomography *ex vivo*

The DOC-Hy NPs were tested for PA tomography in chicken tissue *ex vivo*, as illustrated in Fig. 4(a)-(c). The depth of the loop in the tissue was 1.5 cm in the final chicken tissue phantom. The tube loop was filled with different concentration of the NPs. Fig. 4d presents the reconstructed photoacoustic images of the loop in the phantom. No significant signal was detected from the reference sample of water. The loop with the NPs can be clearly detected even though the concentration is as low as 6.25 $\mu\text{g}/\text{mL}$. The PA signal of the NPs in the reconstructed images presented a concentration-dependent correlation: the NPs with the highest ICG concentration have the strongest PA signal and highest PA image contrast.

4. Conclusions

In the present study, the fluorophore of ICG was successfully assembled on the PSi NPs as J-aggregates with high efficacy (~95%), based on amine silane-assisted metal ion coordination. The effects of metal ions, ion concentration and amine amount on the PA performance of the NPs were studied and optimized. Moreover, DOC was utilized as the 'nanospacer' to create free space for the enhanced intramolecular motion of ICG. Consequently, both photostability and photothermal performance were significantly enhanced in the NPs. Furthermore, the BSA-coated NPs possessed good colloidal stability and biocompatibility. The NPs were detectable at low concentrations with PA tomography at 1.5 cm depth in tissue phantom. Thus, the developed NPs are promising contrast agents for deep tissue PA imaging as well as for light-triggered theranostics. Compared to the complex long-time heating and chemical synthesis applied in literatures, the proposed approach of supramolecular assembly is simple, fast, and scalable. These features are beneficial for large-scale production of the material.

Declaration of Competing Interest

The authors declare that they have no known competing financial interests or personal relationships that could have appeared to influence the work reported in this paper.

Data availability

Data will be made available on request.

Acknowledgements

The financial supports from European Research Council (ERC) (grant agreement No 101001417), Academy of Finland (Project No. 314412, 314411, 336799, 320166) and Finnish Cultural Foundation are acknowledged. The SIB Labs infrastructure unit is acknowledged for the measurements of TEM, UV-Vis and FT-IR.

Appendix A. Supporting information

Supplementary data associated with this article can be found in the online version at [doi:10.1016/j.pacs.2023.100552](https://doi.org/10.1016/j.pacs.2023.100552).

References

- C. Li, L.V. Wang, Photoacoustic tomography and sensing in biomedicine, *Phys. Med. Biol.* 54 (2009) R59.
- L.V. Wang, J. Yao, A practical guide to photoacoustic tomography in the life sciences, *Nat. Methods* 13 (2016) 627–638.
- H.F. Zhang, K. Maslov, G. Stoica, L.V. Wang, Functional photoacoustic microscopy for high-resolution and noninvasive *in vivo* imaging, *Nat. Biotechnol.* 24 (2006) 848–851.
- P. Beard, Biomedical photoacoustic imaging, *Interface Focus* 1 (2011) 602–631.
- I. Steinberg, D.M. Huland, O. Vermesh, H.E. Frostig, W.S. Tummers, S.S. Gambhir, Photoacoustic clinical imaging, *Photoacoustics* 14 (2019) 77–98.
- J. Weber, P.C. Beard, S.E. Bohndiek, Contrast agents for molecular photoacoustic imaging, *Nat. Methods* 13 (2016) 639–650.
- J. Brunker, J. Yao, J. Laufer, S.E. Bohndiek, Photoacoustic imaging using genetically encoded reporters: a review, *J. Biomed. Opt.* 22 (2017), 070901.
- C. Gellini, A. Feis, Optothermal properties of plasmonic inorganic nanoparticles for photoacoustic applications, *Photoacoustics* 23 (2021), 100281.
- K. Li, X. Duan, Z. Jiang, D. Ding, Y. Chen, G.-Q. Zhang, Z. Liu, J-aggregates of meso-[2,2]paracyclophanyl-BODIPY dye for NIR-II imaging, *Nat. Commun.* 12 (2021) 2376.
- W. Chen, C.-A. Cheng, E.D. Cosco, S. Ramakrishnan, J.G.P. Lingg, O.T. Bruns, J. I. Zink, E.M. Sletten, Shortwave infrared imaging with J-aggregates stabilized in hollow mesoporous silica nanoparticles, *J. Am. Chem. Soc.* 141 (2019) 12475–12480.
- A. Hariri, J. Lemaster, J. Wang, A.S. Jeevarathinam, D.L. Chao, J.V. Jokerst, The characterization of an economic and portable LED-based photoacoustic imaging system to facilitate molecular imaging, *Photoacoustics* 9 (2018) 10–20.
- N. Zhang, Y. Xu, X. Xin, P. Huo, Y. Zhang, H. Chen, N. Feng, Q. Feng, Z. Zhang, Dual-modal imaging-guided theranostic nanocarriers based on 2-methoxyestradiol and indocyanine green, *Int. J. Pharm.* 592 (2021), 120098.
- L. Sun, L. Chen, K. Yang, W.F. Dai, Y. Yang, X. Cui, B. Yang, C. Wang, A multiple functional supramolecular system for synergetic treatments of hepatocellular carcinoma, *Int. J. Pharm.* 619 (2022), 121716.
- Y. Li, G. Liu, J. Ma, J. Lin, H. Lin, G. Su, D. Chen, S. Ye, X. Chen, X. Zhu, Z. Hou, Chemotherapeutic drug-photothermal agent co-self-assembling nanoparticles for near-infrared fluorescence and photoacoustic dual-modal imaging-guided chemophotothermal synergistic therapy, *J. Control. Release* 258 (2017) 95–107.
- X. Tan, J. Wang, X. Pang, L. Liu, Q. Sun, Q. You, F. Tan, N. Li, Indocyanine green-loaded silver nanoparticle@polyaniline core/shell theranostic nanocomposites for photoacoustic/near-infrared fluorescence imaging-guided and single-light-triggered photothermal and photodynamic therapy, *ACS Appl. Mater. Interfaces* 8 (2016) 34991–35003.
- Z. Yuan, C. Lin, Y. He, B. Tao, M. Chen, J. Zhang, P. Liu, K. Cai, Near-infrared light-triggered nitric-oxide-enhanced photodynamic therapy and low-temperature photothermal therapy for biofilm elimination, *ACS Nano* 14 (2020) 3546–3562.
- S. Gan, X. Tong, Y. Zhang, J. Wu, Y. Hu, A. Yuan, Covalent organic framework-supported molecularly dispersed near-infrared dyes boost immunogenic phototherapy against tumors, *Adv. Funct. Mater.* 29 (2019) 1902757.
- W. Xu, J. Rytönen, S. Rönkkö, T. Nissinen, T. Kinnunen, M. Suvanto, A. Närvänen, V.-P. Lehto, A nanostopper approach to selectively engineer the surfaces of mesoporous silicon, *Chem. Mater.* 26 (2014) 6734–6742.
- K. Tamarov, S. Näkki, W. Xu, V.-P. Lehto, Approaches to improve the biocompatibility and systemic circulation of inorganic porous nanoparticles, *J. Mater. Chem. B* 6 (2018) 3632–3649.
- J. Kang, D. Kim, J. Wang, Y. Han, J.M. Zuidema, A. Hariri, J.-H. Park, J.V. Jokerst, M.J. Sailor, Enhanced performance of a molecular photoacoustic imaging agent by encapsulation in mesoporous silicon nanoparticles, *Adv. Mater.* 30 (2018) 1800512.
- B. Changalvaie, S. Han, E. Moaseri, F. Scaletti, L. Truong, R. Caplan, A. Cao, R. Bouchard, T.M. Trussett, K.V. Sokolov, K.P. Johnston, Indocyanine green J aggregates in polymersomes for near-infrared photoacoustic imaging, *ACS Appl. Mater. Interfaces* 11 (2019) 46437–46450.
- C.A. Wood, S. Han, C.S. Kim, Y. Wen, D.R.T. Sampaio, J.T. Harris, K.A. Homan, J. L. Swain, S.Y. Emelianov, A.K. Sood, J.R. Cook, K.V. Sokolov, R.R. Bouchard, Clinically translatable quantitative molecular photoacoustic imaging with liposome-encapsulated ICG J-aggregates, *Nat. Commun.* 12 (2021) 5410.
- W. Xu, J. Leskinen, J. Tick, E. Happonen, T. Tarvainen, V.-P. Lehto, Black mesoporous silicon as a contrast agent for LED-based 3D photoacoustic tomography, *ACS Appl. Mater. Interfaces* 12 (2020) 5456–5461.
- H. Aoki, M. Nojiri, R. Mukai, S. Ito, Near-infrared absorbing polymer nano-particle as a sensitive contrast agent for photo-acoustic imaging, *Nanoscale* 7 (2015) 337–343.
- H. Li, H. Wen, Z. Zhang, N. Song, R.T.K. Kwok, J.W.Y. Lam, L. Wang, D. Wang, B. Z. Tang, Reverse thinking of the aggregation-induced emission principle: amplifying molecular motions to boost photothermal efficiency of nanofibers**, *Angew. Chem. Int. Ed.* 59 (2020) 20371–20375.
- Z. Zhao, C. Chen, W. Wu, F. Wang, L. Du, X. Zhang, Y. Xiong, X. He, Y. Cai, R.T. K. Kwok, J.W.Y. Lam, X. Gao, P. Sun, D.L. Phillips, D. Ding, B.Z. Tang, Highly efficient photothermal nanoagent achieved by harvesting energy via excited-state intramolecular motion within nanoparticles, *Nat. Commun.* 10 (2019) 768.
- M. Chen, X. Zhang, J. Liu, F. Liu, R. Zhang, P. Wei, H. Feng, M. Tu, A. Qin, J.W. Y. Lam, D. Ding, B.Z. Tang, Evoking phototherapy by capturing intramolecular bond stretching vibration-induced dark-state energy, *ACS Nano* 14 (2020) 4265–4275.
- S. Schöttler, K. Landfester, V. Mailänder, Controlling the stealth effect of nanocarriers through understanding the protein corona, *Angew. Chem. Int. Ed.* 55 (2016) 8806–8815.
- W. Xu, K. Tamarov, L. Fan, S. Granroth, J. Rantanen, T. Nissinen, S. Peräniemi, O. Uski, M.-R. Hirvonen, V.-P. Lehto, Scalable synthesis of biodegradable black mesoporous silicon nanoparticles for highly efficient photothermal therapy, *ACS Appl. Mater. Interfaces* 10 (2018) 23529–23538.
- E. Happonen, K. Tamarov, M.-V. Martikainen, K. Ketola, M. Roponen, V.-P. Lehto, W. Xu, Thermal dose as a universal tool to evaluate nanoparticle-induced photothermal therapy, *Int. J. Pharm.* 587 (2020), 119657.
- J. Tick, A. Pulkkinen, F. Lucka, R. Ellwood, B.T. Cox, J.P. Kaipio, S.R. Arridge, T. Tarvainen, Three dimensional photoacoustic tomography in Bayesian framework, *J. Acoust. Soc. Am.* 144 (2018) 2061–2071.

- [32] B.E. Treeby, B.T. Cox, k-Wave: MATLAB toolbox for the simulation and reconstruction of photoacoustic wave fields, *J. Biomed. Opt.* 15 (2010) 021314.
- [33] H.T. Ngo, X. Liu, K.A. Jolliffe, Anion recognition and sensing with Zn(II)-dipicolylamine complexes, *Chem. Soc. Rev.* 41 (2012) 4928–4965.
- [34] C. Chu, E. Ren, Y. Zhang, J. Yu, H. Lin, X. Pang, Y. Zhang, H. Liu, Z. Qin, Y. Cheng, X. Wang, W. Li, X. Kong, X. Chen, G. Liu, Zinc(II)-dipicolylamine coordination nanotheranostics: toward synergistic nanomedicine by combined photo/gene therapy, *Angew. Chem. Int. Ed.* 58 (2019) 269–272.
- [35] M.C. Poirier, Chemical-induced DNA damage and human cancer risk, *Nat. Rev. Cancer* 4 (2004) 630–637.
- [36] L. Zhao, Y. Liu, R. Xing, X. Yan, Supramolecular photothermal effects: a promising mechanism for efficient thermal conversion, *Angew. Chem.* 132 (2020) 3821–3829.
- [37] X. Li, X.-H. Peng, B.-D. Zheng, J. Tang, Y. Zhao, B.-Y. Zheng, M.-R. Ke, J.-D. Huang, New application of phthalocyanine molecules: from photodynamic therapy to photothermal therapy by means of structural regulation rather than formation of aggregates, *Chem. Sci.* 9 (2018) 2098–2104.
- [38] M.D. Arning, S.D. Minter, 18 - Electrode Potentials, in: C.G. Zoski (Ed.), *Handbook of Electrochemistry*, Elsevier, Amsterdam, 2007, pp. 813–827.
- [39] P. Xue, M. Hou, L. Sun, Q. Li, L. Zhang, Z. Xu, Y. Kang, Calcium-carbonate packaging magnetic polydopamine nanoparticles loaded with indocyanine green for near-infrared induced photothermal/photodynamic therapy, *Acta Biomater.* 81 (2018) 242–255.
- [40] C.-C. Huang, W. Huang, C.-S. Yeh, Shell-by-shell synthesis of multi-shelled mesoporous silica nanospheres for optical imaging and drug delivery, *Biomaterials* 32 (2011) 556–564.



Wujun Xu is an Adjunct Professor in the Department of Applied Physics, University of Eastern Finland. He received his doctoral degree in Materials Science from the University of Chinese Academy of Sciences (2018). His research interests include novel porous nanomaterials and related biomedical applications.



Vesa-Pekka Lehto is a Professor in the Department of Applied Physics at the University of Eastern Finland. He obtained his PhD from the University of Turku (Finland) in 1999. His research interests include the development of multifunctional porous nanomaterials for nanomedicines, metal adsorption, and anode material for Li-ion batteries.